Quantitative study of amplitude noise effects on dynamical localization

Daniel A. Steck, Valery Milner, Windell H. Oskay, and Mark G. Raizen
Department of Physics, The University of Texas at Austin, Austin, Texas 78712-1081
(Received 16 September 1999)

We study the motion of cold atoms in a pulsed standing wave of light, which constitutes an experimental realization of the quantum kicked rotor. This system exhibits dynamical localization, where quantum effects suppress classical momentum diffusion. As we introduce amplitude noise, the coherences that lead to localization are destroyed, resulting in restored diffusion. For high levels of noise, we find that the experiment is well described by a classical model, suggesting that classical behavior has been restored. We present a detailed experimental study of this noise-induced transition from quantum to classical behavior.

PACS number(s): 05.45.Mt, 42.50.Vk, 32.80.Pj

I. INTRODUCTION

It is well known that quantum effects can suppress chaotic motion in systems with chaotic classical limits [1]. Since this suppression relies on quantum interferences, noise and dissipation can destroy these interferences and restore the expected classical behavior. The destruction of quantum interference, called decoherence, is especially important in reconciling the classical and quantum descriptions of chaotic systems, where simple quantum descriptions predict that nonclassical effects appear after only a short time, even for macroscopic systems [2]. Because of the general importance of decoherence in quantum-classical correspondence, there has been much theoretical work on this subject [2–9].

Despite the vast body of theoretical work on the subject, there have been few experiments dealing directly with decoherence in classically nonintegrable systems. The first studies in this area considered the effects of noise on Rydberg atom ionization [10–14]. Especially relevant to the work presented here are Refs. [11–13], where noise added to the microwave driving of the Rydberg atoms led to an improved agreement with classical predictions of ionization thresholds. There has also been some work investigating the effects of temperature on conductance fluctuations in mesoscopic structures [15]. Finally, there has been preliminary work in atom optics [16,17], which forms the backdrop for the work discussed here.

Although work in chaotic systems has been limited, it should be noted that there have also been some recent experiments on decoherence in linear systems. These experiments include spontaneous emission in atom interferometry [18], decoherence of a coupled Rydberg atom-microwave cavity system [19], and the decoherence of a superposition of motional states in an ion trap [20]. However, there is much left to understand, and more experimental work is needed in both linear and nonlinear systems.

Atom optics has emerged as an important testing ground for ideas in quantum chaos. The initial idea for a quantum chaos experiment in atom optics came in a proposal by Graham, Schlautmann, and Zoller [21], which considered an atomic beam crossing a phase-modulated standing wave of light. An important simplification was made to this basic scheme when it was experimentally realized in our laboratory [22,23], where sodium atoms cooled and confined in a magneto-optic trap (MOT) were subject to a phase-modulated standing wave, with negligible transverse motion. Later, the phase-modulated light was replaced with a pulsed standing wave, leading to an atom-optics realization of the kicked rotor [24], a simpler and more fundamental system for the study of quantum chaos. The experiments described in this paper are performed on a second-generation apparatus, based on cold cesium atoms, which has several advantages that allow for these experiments [25]. In general, atom optics is an ideal setting for these experiments, because one can directly measure the distribution of atomic momentum. Additionally, one has direct and precise control over many experimental parameters, which is especially useful in studying different types of noise and dissipation.

II. THEORETICAL BACKGROUND

A. The kicked rotor in atom optics

The connection between an atom in a standing wave of light and the kicked-rotor problem forms the basis for all the experiments described here. We begin our discussion of this connection by considering the dynamics of a two-level atom in a standing wave of monochromatic light. The optical field is described by a superposition of counterpropagating traveling waves,

$$\mathbf{E}(x,t)=\hat{z}2E_0\cos(k_{\mathrm{L}}x)\cos(\omega_{\mathrm{L}}t), \tag{1}$$

where E_0 is the field amplitude of a single traveling-wave component, ω_{L} is the frequency of the field, and $k_{\mathrm{L}}=\omega_{\mathrm{L}}/c$. This field configuration is the linearly polarized, one-dimensional optical lattice that is now commonly used in atom optics. The dipole interaction leads to a spatially dependent ac Stark shift of the atomic levels. We are interested in the limit where the laser detuning $\Delta_{\mathrm{L}}:=\omega_{\mathrm{L}}-\omega_0$ from the atomic resonance ω_0 is large compared to the excited-state decay rate Γ. In this regime, the dipole force due to the Stark shift can be significant, while incoherent effects such as spontaneous emission and the stochastic dipole force [26] can be made negligibly small. Furthermore, the atom is almost entirely in the ground state; in fact, since we are interested in atomic motion on time scales slow compared to $1/\Delta_{\mathrm{L}}$, we can adiabatically eliminate the excited state of the atom [21]. In this adiabatic approximation, we can ignore the

internal structure of the atom, and treat it as a point particle. The resulting reduced center-of-mass Hamiltonian is

$$H(x,p)=\frac{p^2}{2m}+V_0\cos(2k_Lx), \tag{2}$$

where m is the atomic mass, $V_0:=\hbar\Omega^2/8\Delta_L$ is the ''well depth'' of the lattice, $\Omega:=-2d_zE_0/\hbar$ is the maximum Rabi frequency, and **d** is the atomic dipole moment. (Note that in writing down this Hamiltonian we have also implicitly invoked the dipole and rotating-wave approximations.) This Hamiltonian corresponds to that of the familiar pendulum. In atom optics, this lattice plays the role of a sinusoidal phase diffraction grating.

So far, we have described a realization of the quantum pendulum, which is an integrable system. A more interesting case arises when the well depth is time dependent, and the dynamics are chaotic. Since V_0 is proportional to the intensity of the optical field, this time dependence is easily produced via amplitude modulation of the standing wave. The kicked rotor corresponds to a potential that is periodically pulsed in time:

$$H(x,p,t)=\frac{p^2}{2m}+V_0\cos(2k_Lx)\sum_n F(t-nT). \tag{3}$$

Here T is the kick period, and $F(t)$ is a pulse function of unit height and duration $t_p\ll T$. The δ-kicked rotor corresponds to the limit of δ-function pulses; most theoretical work focuses on this limit because of the tremendous simplification of the equations of motion, as we discuss below. In a physical experiment, however, one can only strive to come as close as possible to this limit by using short, intense laser pulses.

Before proceeding, we can simplify our discussions by transforming to a set of scaled, dimensionless units. If we define

$$\begin{aligned} x' &:= 2k_Lx,\\ p' &:= (\bar{k}/2\hbar k_L)p,\\ t' &:= t/T,\\ f(t') &:= F(t)/\eta,\\ K &:= (\bar{k}/\hbar)\eta TV_0,\\ H' &:= (\bar{k}/\hbar)TH, \end{aligned} \tag{4}$$

then we can rewrite the kicked rotor Hamiltonian [Eq. (3)] as

$$H(x,p,t)=\frac{p^2}{2}+K\cos x\sum_n f(t-n), \tag{5}$$

after dropping the primes. In the above transformations, the parameter K is known as the *stochasticity parameter*; additionally, we have defined the pulse integral $\eta := T^{-1}\int_{-\infty}^{\infty}F(t)dt\propto t_p$ [so that $\int_{-\infty}^{\infty}f(t)dt=1$] and the constant $\bar{k}:=8\omega_rT$, where $\omega_r:=\hbar k_L^2/2m$ is the recoil frequency. In view of the scaled commutation relation $[x,p]=i\bar{k}$, we can interpret $\bar{k}$ as a scaled Planck constant, which measures the action scale of the system, normalized to $\hbar$. Henceforth we will use these scaled variables, with the main exception being that in the presentation of the data we report momentum in multiples of two photon recoils ($2\hbar k_L$). From the second transformation in Eqs. (4), we see that this specification is equivalent to reporting the scaled momentum in multiples of $\bar{k}$. This momentum scale is more natural, since the dipole force results from the scattering of a photon from one traveling wave into the other, and hence the atomic momentum can only change by $2\hbar k_L$ at a time. This momentum ladder also arises naturally from the spatial periodicity of the potential.

One final note is in order, since the cesium atoms we use in the experiment have fairly complicated hyperfine structure, and one may question the accuracy of a two-level atom model. Fortunately, there is a symmetry in the hyperfine structure that simplifies its treatment significantly. In these experiments, it is important to optically pump the atoms into one ground hyperfine level ($F=4$ for our experiments here), which itself has a set of (nearly) degenerate magnetic sublevels. Then, it is important for the detuning to be large, so that the excited-state hyperfine structure is approximately degenerate (for our setup, Δ_L must be large compared to $\sim$0.5 GHz). Since the light is linearly polarized, each ground-state sublevel is independently coupled to its own set of excited-state sublevels. In this case, the sums over the excited-state couplings turn out to be independent of the ground state sublevel. Hence, in the far-detuned, linearly polarized regime, one can use an effective dipole moment $d_{eff}=2.2\times10^{-29}$ C m in place of d_z, and employ the two-level atom model.

B. Classical dynamics

The δ-kicked rotor problem is a paradigm system for the study of classical and quantum chaos. One reason for its importance is the simplicity of the corresponding equations of motion. Since the motion is dominated at any given time by either the kinetic or potential component of the Hamiltonian, Hamilton's equations can be integrated over one temporal period, yielding the standard map [27]

$$\begin{aligned} x_{n+1} &= x_n+p_{n+1},\\ p_{n+1} &= p_n+K\sin x_n. \end{aligned} \tag{6}$$

Here x_n and p_n refer to the momentum just before the nth kick. The simplicity of this mapping has made many analytic as well as numerical studies possible, and much is known about the classical dynamics of the kicked rotor.

The most important aspect of the kicked rotor for our purposes is its global behavior. In our studies, we are interested in the regime of large K (which in practice means $K\gtrsim5$), where the phase space is predominantly chaotic and there are no invariant Kolmogorov-Arnold-Moser (KAM) surfaces that would prevent unbounded motion in p. We will begin our discussion by considering the mean kinetic energy of an ensemble of rotors (see Ref. [7] for a similar discussion, although with slightly different notation). Using the second equation in the standard map [Eq. (6)], we find

$$E_n=\frac{\langle p_n^2\rangle}{2}=\frac{1}{2}\sum_{m,m'=0}^{n-1}C_{m-m'}, \tag{7}$$

where the correlation functions C_m are given by

$$C_{m-m'}:=\langle K\sin x_m K\sin x_{m'}\rangle. \tag{8}$$

The angle brackets denote a uniform average over phase space, and the correlations depend only on the time difference $(m-m')$. The sum in Eq. (7) can be easily evaluated if one makes the approximation that the coordinate x_n is uniform and uncorrelated, as one might expect for very large K when the phase space is almost entirely chaotic. Doing so allows one to ignore the off-diagonal terms and gives the result

$$E_n=\frac{C_0}{2}n=\frac{K^2}{4}n. \tag{9}$$

The energy growth is hence diffusive (linear in time), with diffusion rate $D_{\mathrm{ql}}(K)=K^2/4$, which is known as the *quasilinear* diffusion rate. In fact, this random-phase approximation is equivalent to assuming that the motion is a random walk in momentum, so the momentum distribution is asymptotically Gaussian, with a width $\sim\sqrt{n}$.

The random-phase approximation is only valid as $K\to\infty$, however, and for finite K the higher-order correlations cannot always be neglected, even for trajectories within the chaotic region of phase space. Nonuniformities in the chaotic region, especially in the neighborhood of stability islands, can lead to nonzero correlations, and hence to deviations of the diffusion rate from the quasilinear value. A more general expression for the (time-dependent) diffusion rate in terms of the higher-order correlations is

$$D_n:=E_{n+1}-E_n=\frac{1}{2}\sum_{m=-n}^{n}C_m. \tag{10}$$

These corrections to the diffusion rate were treated analytically in Refs. [28,29], where Eq. (10) was shown to be an asymptotic expansion in powers of Bessel functions of K. The result from Ref. [29] is

$$D(K)=\frac{K^2}{2}\left(\frac{1}{2}-J_2(K)-J_1^2(K)+J_2^2(K)+J_3^2(K)\right), \tag{11}$$

to second order in the Bessel functions. This expression represents the diffusion rate D_n for long times n and large values of K; the higher-order terms in the expansion are assumed at this point to have only a small contribution, since they represent higher powers of $1/\sqrt{K}$. [Note that it is often convenient to neglect $J_3{}^2(K)-J_1{}^2(K)$, which is $O(K^{-2})$, since for large K this difference is much smaller than $J_2{}^2(K)$, which is $O(K^{-1})$; however, these terms will be important when generalizing this result to account for amplitude noise below.] This result shows that $D(K)$ oscillates about the quasilinear value, where the corrections become small compared to the quasilinear value as K becomes large.

The diffusion calculation leading to Eq. (11) took into account only the first few correlations. However, long-time correlations can also play an important role in the dynamics. In the generic case, there are islands of stability in phase space (even for arbitrarily large K), which have boundaries that are ''sticky'' in the sense that trajectories that wander into these sticky regions can remain there for many kicks. Hence even initial conditions within the chaotic region of phase space will eventually wander near islands, and be stuck to them for a possibly long time before breaking away and continuing to diffuse through the chaotic region. In the case of the standard map, there are two types of stability islands: stability islands in the usual sense, which surround a fixed point of the motion, and *accelerator modes* [27,30], which are similar to the usual stability islands but are boosted in momentum on each kick. The accelerator modes are a peculiarity of the standard map, since the phase space structure is periodic in momentum (with period 2π); other systems, including our system with nonzero-duration pulses, can exhibit *quasiaccelerator modes*, which behave like accelerator modes over a bounded region of phase space [30]. This stickiness leads to Lévy-flight behavior [31]: the islands tend to trap trajectories, leading to reduced transport, whereas the accelerator modes lead to streaming (with many correlated steps in momentum), and hence to enhanced transport. This nondiffusive behavior is referred to as anomalous diffusion, and leads to momentum transport of the form $E(t)\sim t^{\mu}$, where the transport exponent $\mu\neq 1$ for anomalous diffusion [32–34]. This anomalous diffusion is dramatically evident [35,36] when the main family of accelerator modes is stable, that is, where K is near $2\pi j$ for positive integer j. [Note that these locations coincide with the peaks of Eq. (11).] Since the motion is not strictly diffusive, the proper framework for the kicked-rotor transport is fractional kinetics [36–38]. However, since the stable islands in phase space are typically small for large K, it may take many kicks before the islands cause large deviations from diffusive behavior. Hence, for the time scales observed in our experiments (up to 80 kicks), it is appropriate to describe the classical dynamics as diffusive as long as large accelerator modes are not present. Operationally, Eq. (11) is an excellent approximation away from the main family of accelerator modes.

Since we apply amplitude noise to the interaction potential in our experiment, it is important to consider the effect of this noise on the classical dynamics. In this case, the kick strength K is replaced by $K+\delta K_n$, where δK_n is a random deviation for the amplitude of the nth kick. We consider exclusively the case of uniform amplitude noise, which is characterized by the probability distribution

$$P(\delta K)=\begin{cases}1/\delta K_{\text{p-p}}, & \delta K\in(-\delta K_{\text{p-p}}/2,\delta K_{\text{p-p}}/2)\\ 0 & \text{elsewhere,}\end{cases} \tag{12}$$

where $\delta K_{\text{p-p}}$ is the peak-to-peak deviation of the kick strength. When we quote the noise level used in our experiments, we are quoting the normalized peak-to-peak deviation $\delta K_{\text{p-p}}/K$. The noise modifies the correlations, and the generalization of Eq. (8) is

$$C_{m-m'}=\int d(\delta K_m)\cdots d(\delta K_{m'})P(\delta K_m)\cdots P(\delta K_{m'})\times\langle(K+\delta K_m)\sin x_m(K+\delta K_{m'})\sin x_{m'}\rangle, \tag{13}$$

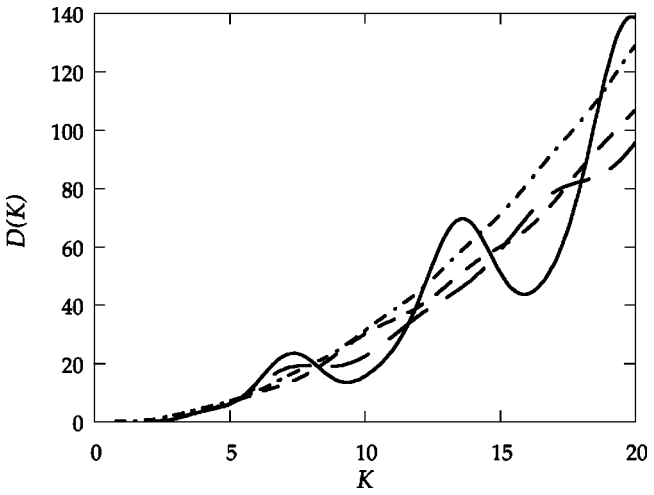

FIG. 1. Plot of diffusion expression (14) for several levels of uniform amplitude noise: no noise (solid line), 50% noise (dashed line), 100% noise (short dashes), and 200% noise (dot-dashed line). The oscillations, which represent short-term correlations, are smoothed out by the noise.

where there are $|m-m'|+1$ integrals over the kick probability distribution, since the coordinate at the later time depends on all the kicks after the earlier time. It is difficult to evaluate this expression directly, but fortunately it is straightforward to generalize the diffusion result in Ref. [29] to include amplitude noise by taking the K associated with each step in the Fourier paths to be an independent random kick of strength $K+\delta K_n$; then each kick strength must be averaged with respect to its probability distribution. Doing so, we arrive at the generalization of Eq. (11):

$$D(K)=\frac{K^2+\mathrm{Var}(\delta K)}{4}+\frac{K^2}{2}(-\mathcal{J}_2(K)-\mathcal{J}_1{}^2(K)+\mathcal{J}_2{}^2(K)+\mathcal{J}_3{}^2(K)). \tag{14}$$

In this equation, $\mathrm{Var}(\delta K)$ denotes the variance of $P(\delta K)$ [which is simply $(\delta K_{\text{p-p}})^2/12$ for uniform noise], and

$$\mathcal{J}_n(K):=\int_{-\infty}^{\infty}P(\delta K)J_n(K+\delta K)d(\delta K). \tag{15}$$

This expression makes it immediately clear how the noise affects the diffusion rate: the integral in Eq. (15) is analogous to a convolution of the Bessel functions with the noise distribution. As the noise level is increased, the Bessel functions are smoothed out, and the correlations are effectively destroyed. This is especially true for long-term correlations, and indeed anomalous diffusion is suppressed in the presence of noise. At the same time, there is an increase in the quasilinear diffusion component [the first term in Eq. (14)], but this effect is generally small in comparison to the destruction of the correlations. For illustration, function (14) is plotted for several different levels of amplitude noise in Fig. 1. Note that for the 100% and 200% noise levels, the correlations are essentially destroyed, so that these noise levels cannot be considered perturbative; however, these noise levels are still small in the sense that their contribution to the quasilinear diffusion rate is significantly smaller than the zero-noise component.

Finally, we note briefly the effects of nonzero pulse widths, which are inherent in a physical experiment. Essentially, the δ-kick approximation breaks down when a rotor is moving sufficiently quickly that one cannot neglect its motion during the kick. At these speeds, the rotor samples an interval of the sinusoidal potential during the kick, and in a similar manner to the destruction of the correlations by noise, the strength of the potential is effectively reduced. The worst possible case is when the rotor moves over a period of the potential during the kick, in which case it experiences no net kick. This effect sets an effective upper momentum boundary for the dynamics. In our experiments, we can minimize this effect by choosing a sufficiently short pulse so that the momentum boundary is far above the highest momenta achieved in the experiments. We will return to this effect when we discuss the systematic effects in the experiment. For a more comprehensive discussion, as well as direct measurements of the effect on our measured momentum distributions, see Ref. [25], as well as the earlier theoretical treatment of Ref. [39].

C. Quantum dynamics

The quantum dynamics of the kicked rotor, first discussed in the seminal work of Ref. [40], are strikingly different in nature from the classical dynamics. In contrast to the diffusive nature of the classical dynamics, the quantum system exhibits diffusive behavior for only a short time, called the *quantum break time*, after which the diffusion is suppressed. In fact, this suppression of diffusion is symptomatic of a more fundamental difference between the quantum and classical systems, as shown through elegant time-reversal simulations by Shepelyansky [41]: the quantum dynamics are stable (quasiperiodic) and not chaotic, in stark contrast to the classical dynamics. This stability can also be seen from the (locally) discrete quasienergy spectrum of the kicked rotor [42–44]. Hence it is clear that quantum effects suppress classical chaos in the kicked rotor, and this quantum suppression of chaos is referred to as *dynamical localization*. Although much of the theoretical work on this phenomenon has focused on the kicked-rotor problem, dynamical localization also occurs in many other systems [45].

Fishman, Grempel, and Prange [43–45] made an important step forward in the understanding of the quantum kicked rotor by mapping it onto the problem of Anderson localization. One consequence of this analysis was the realization that the quasienergy states (Floquet states) are exponentially localized in momentum. This result provides a useful context for understanding dynamical localization, since the evolution to a localized state can be viewed as a dephasing of the quasienergy states. An initial momentum distribution that is narrow compared to a typical quasienergy state must be a coherent superposition of quasienergy states. As time progresses, the different phase evolutions of the quasienergy basis states result in diffusive behavior for short times. At long times, when the basis states have completely dephased, the distribution relaxes to an incoherent sum of the exponentially localized basis states, resulting in an exponentially localized distribution. For very long times, one also expects quantum recurrences as the basis states rephase [42], but these time scales are far beyond what we can observe experimentally. The suppression of diffusion, as well as the char-

acteristic exponential distributions of dynamical localization, were observed experimentally in Ref. [24] for the kicked rotor, and in Refs. [22,23] for a similar system.

The quantum dynamics can also be understood in terms of the modification of the correlations due to quantum effects. Shepelyansky showed numerically [41] and analytically [46] that, whereas the classical correlations drop off quickly with time (when any residual stable structures are too small to affect the dynamics on a short time scale, i.e., away from the accelerator modes), quantum correlations persist for much longer times. In contrast, for cases of smaller K, and hence more stability, the quantum and classical correlations were similar after the break time. This difference in the correlations is intuitively clear from Eq. (10); in fact, the long-time quantum correlations near the break time must be negative, bringing this sum to nearly zero, in order for the system to exhibit localization.

Shepelyansky also made another observation regarding the quantum correlations that is important for our results presented here. In particular, he calculated the first few quantum correlations, and found that they had the same form as the corresponding classical correlations upon the substitution [47,46,7]

$$K \rightarrow K_{\mathrm{q}} := \frac{\sin(\bar{k}/2)}{\bar{k}/2} K. \tag{16}$$

[Note, however, that the correlations used in Ref. [47] were defined without the factor of K^2 that appears in Eq. (8).] Hence a good approximation for the initial quantum diffusion rate (in the absence of noise) is

$$D(K,\bar{k}) = \frac{K^2}{2}\left(\frac{1}{2} - J_2(K_{\mathrm{q}}) - {J_1}^2(K_{\mathrm{q}}) + {J_2}^2(K_{\mathrm{q}}) + {J_3}^2(K_{\mathrm{q}})\right), \tag{17}$$

where it is assumed that the initial quantum distribution is approximately uniform over a $2\pi \times 2\pi$ unit cell in the classical phase space. Consequently, there is an oscillatory dependence of the initial quantum diffusion rate on K_{q} that is closely related to the underlying classical dynamics. However, the oscillations are shifted due to the quantum scaling factor in Eq. (16). Since the width of the localized distribution (the *localization length*) is related to the initial diffusion rate [47], the oscillations are also apparent in the long-time quantum distributions. This oscillatory structure was observed, and the quantum scaling was confirmed experimentally in Ref. [48], where it was also observed that exponentially localized distributions do not occur for values of K_{q} that lead to maxima in Eq. (17). The quantum scaling factor is significant for the data reported in this paper; typically, we use $\bar{k} = 2.08$, which leads to a quantum shift of the oscillations by about 20% in K.

We now turn to the concept of adding noise to the quantum-kicked rotor. Since the deviation from the classical dynamics is due primarily to long-time correlations, dynamical localization should be susceptible to noise and dissipation, either of which would lead to the destruction of these correlations. Note that noise and dissipation are fundamentally different in nature: noise is a unitary process, and is hence reversible in principle, whereas dissipation is an interaction with a very large (i.e., possessing many degrees of freedom) external system (reservoir), which is an inherently irreversible process. However, noise has essentially the same effect, and we chose to implement it in these experiments because of the high degree of experimental control over the interaction potential. The first study of the influence of noise on the quantum kicked rotor appeared in Ref. [41], where it was observed that a sufficiently strong random perturbation could restore diffusion at the classical rate. Soon thereafter, a more detailed theoretical treatment was presented by Ott, Antonsen, and Hanson [4], who showed that if the scaled Planck constant is sufficiently small, classical diffusion is restored, even for small amounts of added noise. Some restored diffusion was observed previously in the kicked rotor in the presence of amplitude noise [16] and in the presence of spontaneous emission [16,17], but in these experiments it was not clear whether the behavior had returned to the classical limit.

To reach the classical limit in our experiment, the short-term correlations must also be modified by the noise, in view of the quantum scaling factor in Eq. (16), which as mentioned before is significant for our typical parameter values. One can generalize the work of Shepelyansky leading to Eq. (17) to include amplitude noise, with the result

$$D(K,\bar{k}) = \frac{K^2 + \mathrm{Var}(\delta K)}{4} + \frac{K^2}{2}\left(-\mathcal{Q}_2(K_{\mathrm{q}}) - {\mathcal{Q}_1}^2(K_{\mathrm{q}}) + {\mathcal{Q}_2}^2(K_{\mathrm{q}}) + {\mathcal{Q}_3}^2(K_{\mathrm{q}})\right), \tag{18}$$

where

$$\mathcal{Q}_n(K_{\mathrm{q}}) := \int_{-\infty}^{\infty} P(\delta K) J_n(K_{\mathrm{q}} + \delta K_{\mathrm{q}}) d(\delta K), \tag{19}$$

and $\delta K_{\mathrm{q}} = \delta K \sin(\bar{k}/2)/(\bar{k}/2)$. Thus the short-time quantum correlations are washed out in much the same way as the classical correlations, as in Eq. (14). However, since the locations of the classical and quantum oscillations in $D(K)$ are different for our operating parameters, we can immediately conclude that in order to observe good correspondence between quantum and classical evolution, the applied noise must be very strong. In this case, both quantum and classical diffusion will proceed at the quasilinear rate, since the diffusion oscillations will be destroyed (as in Fig. 1), and the global behavior will be the same. For lower levels of noise, one might expect to recover diffusive behavior in the quantum system (if the long-time correlations responsible for localization are destroyed), but possibly at a rate that does not match the classical prediction.

Finally, we note that amplitude noise is ''ladder preserving,'' which means that atoms can still only change momentum by $2\hbar k_{\mathrm{L}}$ at a time. Other types of noise and dissipation, such as spontaneous emission, can break this ladder symmetry, and possibly lead to more effective destruction of localization [7].

III. EXPERIMENTAL METHOD

The experimental setup is that of our earlier quantum chaos experiments [16,25,48], with minor modifications. A general schematic of the setup is shown in Fig. 2. The ex-

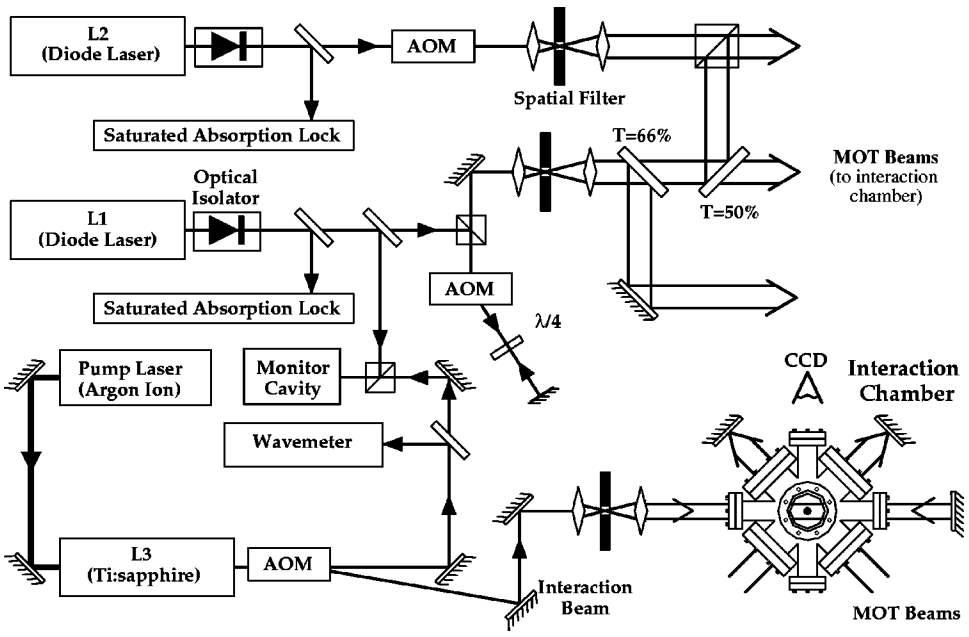

FIG. 2. Schematic diagram of the experimental setup. Two diode lasers provide the light for the MOT, and a Ti:sapphire laser provides the far-detuned standing wave.

periments are performed on laser-cooled cesium atoms in a MOT [49]. Two actively locked, single-mode diode lasers (L1 and L2) at 852 nm are used for cooling, trapping, and detection of the cesium atoms. The main beam from L1 is double passed through a tunable acousto-optic modulator (AOM) that provides fast control over the intensity and detuning of the beam. During the trapping stage of the experiment, the light from L1 is locked 15 MHz to the red of the $(6S_{1/2},F=4)\rightarrow(6P_{3/2},F=5)$ cycling transition. This light is collimated with a radius of 11 mm, and has a typical power of 23 mW at the chamber. The light from L1 is split into three beams that are retroreflected through the center of the chamber in a standard six-beam MOT configuration. The second laser, L2, is locked to the $(6S_{1/2},F=3)\rightarrow(6P_{3/2},F=3,4)$ crossover transition, and shifted onto the $(6S_{1/2},F=3)\rightarrow(6P_{3/2},F=4)$ resonance with an AOM that also provides fast control over the intensity of the beam. This beam prevents optical pumping into the $F=3$ ground state during the trapping and detection stages.

After trapping and initial cooling, the intensity of L1 is reduced for 7 ms, and the detuning is increased to 55 MHz to further cool the sample. After this final cooling, the trapping fields are then turned off. The light from L2 is left on 150 μs longer than the light from L1, to ensure that the atoms are left in the $(6S_{1/2},F=4)$ ground state. Typically, we trap 10^6 atoms with $\sigma_x=0.15$ mm and $\sigma_p/2\hbar k_{\mathrm{L}}=4$ (determined by fitting a simple Gaussian model). The momentum distribution in the trap is mostly Gaussian, with broadened tails. Similar distributions were observed by other groups, especially for strong magnetic-field gradients (e.g., Refs. [50,51]). A reasonably good model for this momentum distribution is an incoherent sum of a Gaussian and an exponential distribution:

$$\eta_{\mathrm{g}}\frac{1}{\sqrt{2\pi}\sigma_p}\exp\left(-\frac{p^2}{2\sigma_p^2}\right)+\eta_{\mathrm{e}}\frac{1}{2\xi_p}\exp\left(-\frac{|p|}{\xi_p}\right). \qquad (20)$$

A typical measured distribution is plotted in Fig. 3, along with function (20). The parameters for the model were determined from a best fit; the widths of the components are $\sigma_p/2\hbar k_{\mathrm{L}}=3.9$ and $\xi_p/2\hbar k_{\mathrm{L}}=13.0$, and the relative weights are $\eta_{\mathrm{g}}=82\%$ and $\eta_{\mathrm{e}}=18\%$. This distribution corresponds to the initial conditions for all our kicked rotor experiments. We mention this model only to more precisely quantify our initial conditions. For the simulations described before, we construct the initial conditions directly from the experimental data. It should be noted that the choice of an exponential distribution to model the broad tails is purely empirical, and is in no way related to the exponential localization that is observed after several kicks in the kicked-rotor evolution. Using a simple Gaussian model for our measured distribu-

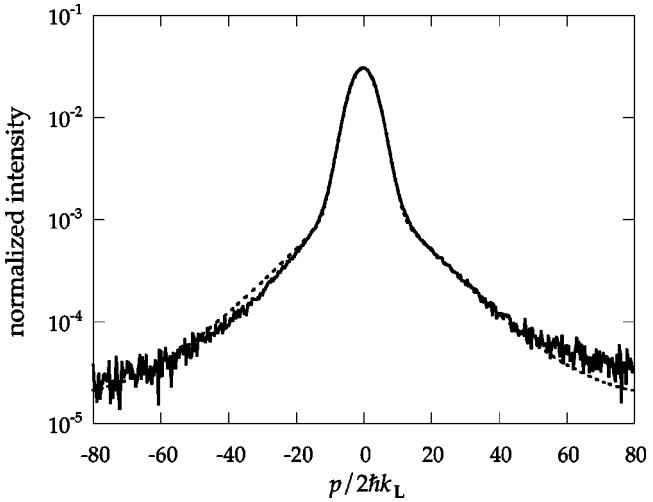

FIG. 3. Plot of the momentum distribution in the MOT (solid line), with model distribution (20) (dotted line). Most of the atoms are in the main Gaussian component, while a smaller fraction is contained in the broad, non-Gaussian tails. This distribution corresponds to the initial conditions of our kicked-rotor experiments.

tion, we find that 96% of the atoms are accounted for by this thermal model, with the remaining 4% augmenting the tails of the momentum profile.

Once the trapping light is off, the interaction potential is turned on. The pulsed standing wave is provided by a stabilized single-mode Ti:sapphire laser (L3). The light from L3 passes through a third AOM that controls the pulse sequence. The linearly polarized beam is spatially filtered, aligned with the atoms, and retroreflected through the chamber to form a standing wave. The beam has a typical maximum power of 470 mW at the chamber, and a waist of 1.5 mm. For all the experiments described here, this beam is detuned 6.1 GHz to the red of the cycling transition, with typical fluctuations of about 100 MHz. The frequency of this laser is monitored by a wavemeter (scanning Michelson interferometer), which has a resolution of around 500 MHz; the frequency is also monitored on a finer scale (with a resolution of around 10 MHz) by comparing it to the light from L1 on a scanning Fabry-Perot cavity. The pulse sequence consists of a series of 295-ns (full width at half maximum) pulses with a rise-fall time of 70 ns, and less than a 3-ns variation in the pulse duration. The pulse period used for these experiments was $T=20\ \mu$s, with variations of less than 4 ns. This period corresponds to $\bar{\kappa}=2.08$. The detection of momentum is accomplished by letting the atoms drift in the dark for a controlled duration (typically 15 ms). The trapping beams are then turned on in zero magnetic field, forming an optical molasses that freezes the position of the atoms. The atomic position is recorded via fluorescence imaging in a short (10 ms) exposure on a cooled charge-coupled device (CCD). The final spatial distribution and the free-drift time enable the determination of the one-dimensional momentum distribution.

We now briefly discuss the dominant systematic uncertainties in our experiment. The uncertainty in the spatial calibration of our imaging system leads to an uncertainty of 2% in the measured momenta, and hence 4% in the measured energies. The uncertainties in the power meter and beam diameter measurements lead to a 10% systematic uncertainty in the mean kick strength. While the locations of the oscillations in Eq. (17) provide, in principle, an *in situ* calibration of the laser intensity, the uncertainty in this method is at the same level, since the effects presented in Sec. IV strongly modify the measured energies, and it is difficult to account for these effects in a quantum model of the experiment. Even worse, the kick strength exhibits long-term drifts due to drifts in the laser intensity and detuning, alignment with the spatial filter, and alignment with respect to the atoms. These drifts occur on time scales of minutes to hours, and can cause systematic shifts in local sections of a data set, since a typical data run can last many hours. It is particularly important to keep this point in mind when comparing the data to classical models, since the error bars shown with the data represent statistical scatter among measurements at the same set of parameter values, but they cannot properly account for these long-term drifts. There are several other effects that impact the measurements of momentum distributions and distribution energies, and we discuss them in detail in Sec. IV as well as describe how we account for them in our analysis.

IV. CLASSICAL MODEL OF THE EXPERIMENT

In order to facilitate an accurate comparison of the experimental data to the classical limit of the kicked rotor, we perform classical Monte Carlo simulations of the experiment. In these simulations, a large number (typically 2×10^5) of classical trajectories are computed, each with a distinct realization of amplitude noise; momentum distributions and distribution energies are then extracted from this ensemble. Additionally, we account for several different systematic effects that are present in our experiment, in order to provide the best possible classical baseline for comparison. In the remainder of this section we describe in detail each of the systematic effects that we have accounted for, and how we have included them in the comparison of the data to theory.

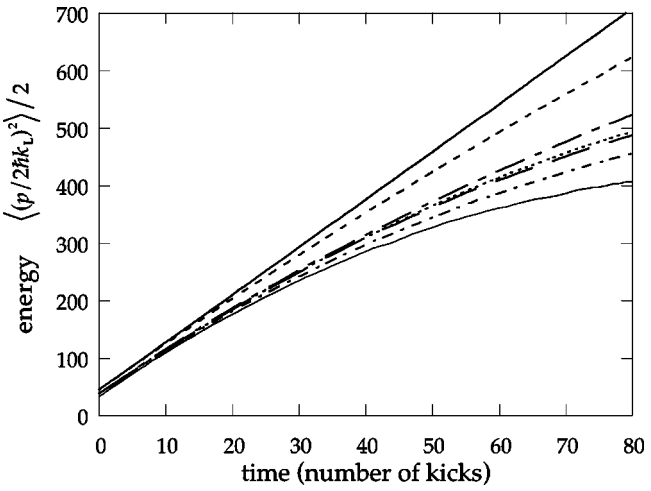

FIG. 4. Example of how the systematic effects described in the text can affect the measured energies. Shown are the simulated average energy evolution for typical operating parameters ($K=11.2$, 100% noise level) and typical parameters for the systematic corrections. The solid straight line is the ideal case, corresponding to the δ-kicked rotor with no corrections; the successively lower curves represent the cumulative result as each effect is accounted for (in the order of presentation in the text): nonzero pulse duration (dashed line), MOT (detection) beam profile (long dot-dashed line), clipping due to the width of the CCD chip (dotted line), profile of interaction beam and transverse atomic motion (long dashes), correction for free-expansion measurement (dot-dashed line), and vertical-offset bias (thin solid line).

The effects that we will describe in this section are illustrated in Fig. 4. This plot compares the energy evolution for different cases where different corrections are accounted for. As each correction is (cumulatively) taken into account, the resulting energy curve is lower and less linear. Indeed, there is quite a large difference between the uncorrected, linear δ-kick curve that one might expect to observe and the fully corrected curve. Hence the importance of this rather technical discussion of experimental details is clear: without carefully taking into account these systematic effects, one might mistakenly attribute curvature in the experimental energy data to residual quantum effects. It is also important to emphasize that although these effects cause a reduction in the dynamic range of the experimental measurements, they do not change the underlying physics in a fundamental way. Finally, we note that most of these systematic effects are such that it is either impractical or impossible to compensate for them with a correction to the experimental data. In this sense, the ''energies'' that we use in our comparisons are not

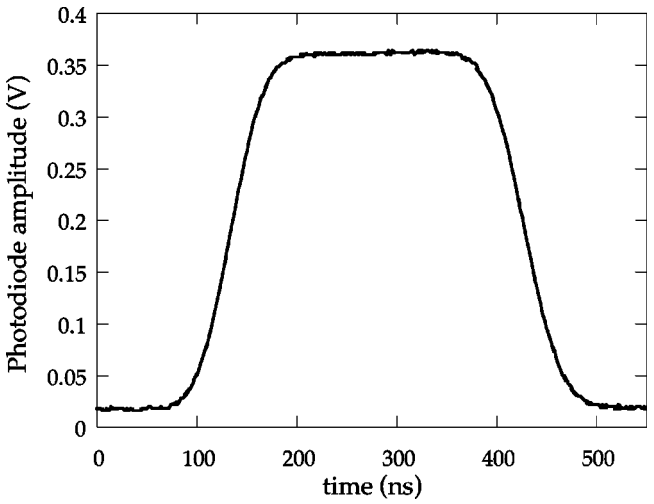

FIG. 5. Model function [Eq. (21)] for the experimental pulses (dashed line) compared to an actual experimental pulse as measured on a fast photodiode (solid line). The two curves are nearly indistinguishable.

true energies, but relatively complicated functions of the true energies and many experimental parameters. Hence it is the ability to take these effects into account in the classical simulations that allows for a quantitative comparison between our experiment and classical theory.

The first, and perhaps most important, effect that we account for is the detailed pulse shape $f(t)$ of our kicks. The nonzero temporal width of the pulses leads to an effective reduction in the kick strength at higher momenta [25], and so it is important to accurately model the experimental pulses in order to reproduce the correct tails in the momentum distributions. It turns out that our experimental pulses are well modeled by the function

$$f(t)=\frac{1}{2\,\eta_{\mathrm{erf}}}\left[\mathrm{erf}\left(\frac{(t-t_1)\sqrt{\pi}}{\delta t_1}\right)-\mathrm{erf}\left(\frac{(t-t_2)\sqrt{\pi}}{\delta t_2}\right)\right], \quad (21)$$

where $t_2-t_1=295$ ns is the full width at half maximum of the pulse, $\delta t_1=67$ ns is the rise time of the pulse (defined such that a straight line going from 0 to 100% of the pulse height in time δt_1 matches the slope of the rising edge at the half-maximum point), $\delta t_2=72$ ns, $\mathrm{erf}(x) \coloneqq(2/\sqrt{\pi})\int_0^x \exp(-t^2)dt$ is the error function, and η_{erf} is a normalization factor, which has the value t_2-t_1 for small values of $\delta t_{1,2}/(t_2-t_1)$. Function (21) is plotted along with a measured optical pulse in Fig. 5. It should be noted that although the agreement between the pulse model and the experimentally measured pulses is excellent, Eq. (21) is merely an empirical model of our observed pulse profiles. In the simulations, the classical equations of motion are directly integrated, using Eq. (21) for the kick profile.

The next effect that we consider is due to the Gaussian profile of the optical molasses laser beams. Recall that to measure momentum distributions, we image the light scattered by the atoms from the molasses beams after a free expansion time. Since the light is not uniform over the atomic cloud, the scattering rate due to atoms with momentum p is given by

$$R_{\mathrm{sc}}=N(p)\left(\frac{\Gamma}{2}\right)\frac{I(x)/I_{\mathrm{sat}}}{1+4(\Delta/\Gamma)^2+I(x)/I_{\mathrm{sat}}}, \quad (22)$$

where $N(p)$ is the number density of atoms with momentum p, $I(x)$ is the local intensity at spatial position x, Γ is the excited state decay rate, and I_{sat} is the saturation intensity ($=2.70$ mW/cm^2, assuming isotropic pumping on the trapping transition). Also, in the free expansion measurement, the unscaled variables x and p are related by $x=v_{\mathrm{r}}(p/\hbar k_{\mathrm{L}})t_{\mathrm{drift}}$, where $v_{\mathrm{r}}=3.5$ mm/s is the velocity corresponding to a single photon recoil, and t_{drift} is the free drift time of the momentum measurement. The spatial intensity profile of the six beams is given by

$$I(x)=2I_0[e^{-2x^2/{w_0}^2}+2e^{-(x^2+2z^2)/{w_0}^2}], \quad (23)$$

where I_0 is the intensity at the center of one of the six beams, $w_0=11$ mm is the beam radius parameter of the Gaussian beams, z is the vertical position of the atoms (transverse to the standing wave, in the direction of gravity), the first term represents the two vertical beams, and the last term represents the four horizontal beams, each at 45° to and in the horizontal plane with the standing wave. Hence, to account for this effect, we apply a correction to the classical simulation of the form

$$f_{\mathrm{mol}}(x)=\frac{f_{\mathrm{I}}(x)}{c_2+f_{\mathrm{I}}(x)}, \quad (24)$$

where $f_{\mathrm{I}}(x)=I(x)/2I_0$ is a scaled intensity profile, and $c_2=[1+4(\Delta/\Gamma)^2][I_{\mathrm{sat}}/(2I_0)]$. The value of c_2 was determined to be 5.94 by fitting correction (24) to a known exponentially localized distribution for various drift times; this value is in reasonable agreement with the expected value of c_2 from the laser parameters.

The finite extent of our imaging CCD camera chip also has an impact on our measurements. We have set up our imaging system such that a typical localized distribution is just contained within the imaged area after a 15-ms drift. However, for strongly noise-driven cases, the momentum distribution can extend significantly past the edges of the imaged area. This effect has little impact on the measured momentum distributions, since it only restricts the measurable range of momentum. However, the energies computed from this momentum distribution are sensitive to this truncation, even if the population in the truncated wings is small. The result is a systematic reduction in the measured energy. It is straightforward to model this effect in the simulations by rejecting trajectories that fall outside the experimental window.

Another effect we must account for is the transverse position of the atoms in the standing-wave beams. Although the spatial size of the beam (with $1/e^2$ radius $w_0=1.5$ mm) is large compared to the size of the initial MOT cloud ($\sigma_x=0.15$ mm), the variation in kick strength over the atomic distribution must be accounted for, especially as the experiment progresses and the atoms move further out transversely. Hence each atom ''sees'' an effective kick strength of $K_{\max}\exp[2(y(t)^2+z(t)^2)/w_0^2]$, where the transverse coordinates y and z are given in scaled units by

$$y(t)=y_0+p_{y0}t,$$
$$z(t)=z_0+p_{z0}t-gt^2/2. \tag{25}$$

In these equations, we have used the scaled gravitational acceleration g, which is related to the acceleration in physical units by $g=2k_{\mathrm{L}}T^2g_{\mathrm{phys}}$. In the simulations, each particle is given initial transverse positions y_0 and z_0 according to a Gaussian distribution that matches the measured MOT size, and initial momenta p_{y0} and p_{z0} that match the momentum distribution measured along the standing wave. It should be noted that this correction may actually increase or decrease the final energies compared to an uncorrected simulation using the mean value of K, even though the mean value of K effectively decreases with time. This is because a subset of the atoms may completely dominate the diffusion if they are located more closely to one of the maxima of $D(K)$. For our parameters, there is typically a spread in K of around 5% in our initial distribution.

Additionally, we must account for a systematic effect that occurs in our free-expansion measurement technique. This technique relies on allowing the atomic cloud to freely expand for 15 ms after the interaction with the standing wave in order to convert the spatial distribution of the atoms into an effective momentum distribution. However, the interaction with the standing wave lasts as long as 1.6 ms for these experiments. Since we define the drift time as the time from the beginning of the standing-wave interaction to the beginning of the camera exposure, the drift time effectively becomes smaller as the number of kicks in the experiment increases. There is no simple way to correct for this effect directly, so we include this effect in our simulations by simulating the free-expansion process. The initial spatial distribution is chosen (in scaled units) to be uniform in the range $[-\pi,\pi)$, which is extremely small compared to the spatial distribution after the expansion. We do not choose the distribution from the MOT spatial distribution to account for convolution effects; these effects have been approximately accounted for already, since the initial momentum distribution used in the simulations is the measured momentum distribution, which is already convolved with the initial spatial distribution. Then the effective momentum of each particle measured by the free-expansion method is

$$p_{\mathrm{eff}}(t)=x(t)+\left(\frac{t_{\mathrm{drift}}-t}{t_{\mathrm{drift}}}\right)p(t), \tag{26}$$

where all quantities are scaled.

The final effect that we account for is due to variations in the background levels measured by our camera. Although we perform background subtraction, which greatly improves our signal-to-noise ratio, the offset levels after the subtraction are generally nonzero, due to fluctuations (from drifts in the camera electronics) and constant offsets (from physical effects in the imaging of the atomic cloud). To enhance the reproducibility of our data, we use the following procedure to fix the zero level of our measured distributions: the 40 lowest points (out of 510 total) in the distribution are averaged together and defined to be the zero level. The disadvantage of this technique is that it results in a slight negative bias in the offset level from the ''true'' distribution. For typical measurements of localized distributions, the bulk of the distribution is contained well within the imaged region. In these cases, the measured values near the edges of the imaged region are small compared to those in the center of

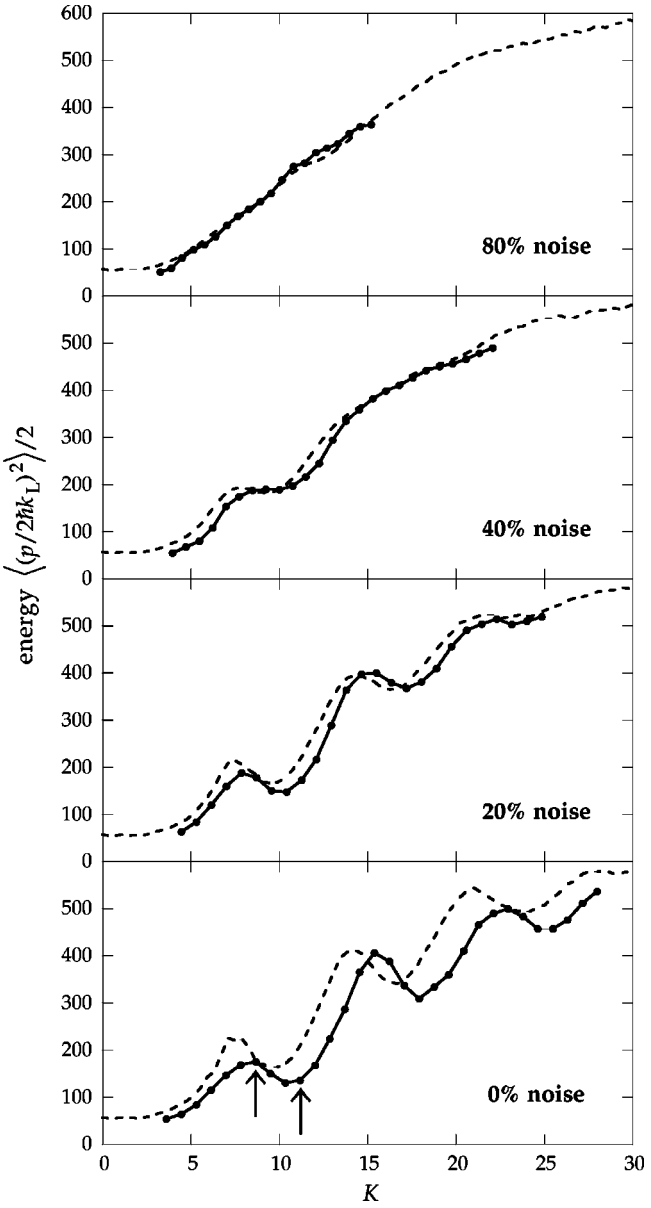

FIG. 6. Plot of experimentally measured energy (points connected by solid lines) and energy from the classical model (dashed line) as a function of the stochasticity parameter K, for several different levels of applied amplitude noise. All the plotted energies are taken at the fixed time of 35 kicks. The oscillations and the shift due to quantum effects, corresponding to Eqs. (11) and (17) with $\bar{\kappa}=2.08$, are clearly apparent in the case with no applied noise. On average, the experimental energies are lower than their classical counterparts due to localization effects for small noise levels. However, for the strongest noise level shown here (80%), there is good agreement between the two energy curves. For this figure, no adjustments have been made to the measured values of K, and the error bars for the energy values are suppressed, but are typically smaller than the corresponding dots. Each experimental point is an average over ten realizations of amplitude noise. Two arrows in the zero-noise case mark the locations of detailed study that are described in the following two subsections.

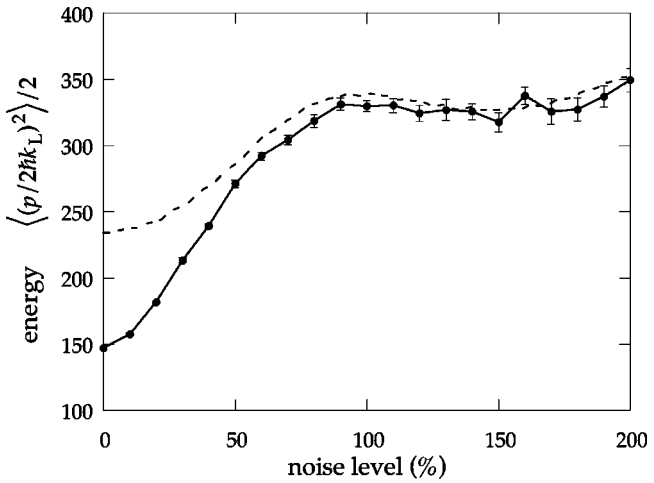

FIG. 7. Experimentally measured energy (points and solid lines) and energy from the classical model (dashed line) as the noise level is changed, for a fixed time (50 kicks) and stochasticity parameter (the experimental value is $K=11.2\pm10\%$, and the classical simulation corresponds to $K=10.9$). At the lowest noise levels, there is a significant difference between the experimental and classical energies, due to both localization and differences in short-term correlations, which disappears for high noise levels. Error bars represent the statistical scatter among the 18 noise realizations comprised in each point, but do not account for long-term drifts or systematic uncertainties (see the note in the text). The value of K used here corresponds to the rightmost arrow in Fig. 6.

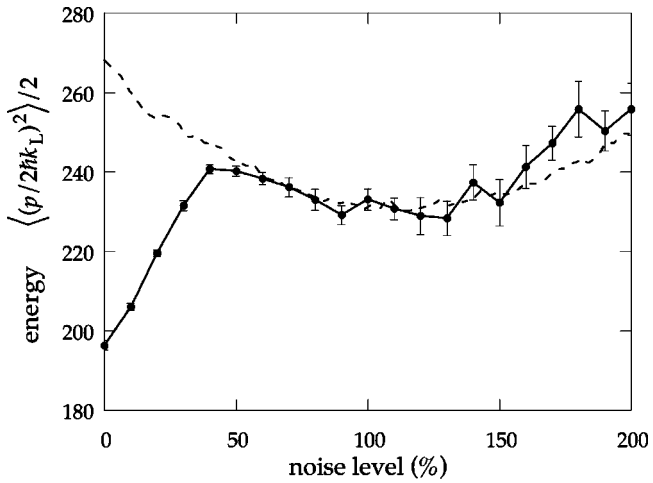

FIG. 8. Experimentally measured energy (points and solid lines) and energy from the classical model (dashed line) as the noise level is changed, for a fixed time (50 kicks) and stochasticity parameter (the experimental value is $K=8.4\pm10\%$, and the classical simulation corresponds to $K=8.4$). As in the case of Fig. 7, there is a large discrepancy between the experimental and classical energies at the lowest noise levels, which disappears for high noise levels. Experimental data are averaged over 18 realizations of noise. The value of K used here corresponds to the leftmost arrow in Fig. 6. Note the larger discrepancy for zero noise in this figure, since the time displayed here is later than that used in Fig. 6. Note also that the vertical scale used here is magnified compared to that of Fig. 7.

the distribution, and the error in the offset is negligible. However, for strongly noise-driven cases, a significant fraction of the distribution can fall outside the imaged region, as noted above. The lowest 40 values are then significantly different from the true zero level, and our procedure can introduce a significant bias. It is straightforward to mimic this process in the simulations, but in some data sets it is possible to restore the correct offset level. For our typical studies of the transition from localized to delocalized behavior, the only cases that are significantly biased are the strongly noise-driven cases, which behave essentially classically (as we will see later). Then one can assume that the biased cases can be modeled as Gaussian distributions, with the MOT beam profile correction applied to them, and we obtain the correct offset by fitting the model function to the measured distribution. This ansatz is justified by the essentially perfect fit of the model function whenever its use is appropriate. Using this idea, we have implemented an automatic procedure for restoring the correct offset in the data sets where the procedure is sensible (Figs. 7–12). In other data (Fig. 6), such as measurements of exponentially localized distributions with very long localization lengths, such a procedure is clearly inappropriate, and this effect is instead accounted for in the corresponding simulations.

There are a few other effects that we do not account for, including spontaneous emission, the stochastic dipole force [26], collisions between atoms, and other sources of noise, most notably phase jitter in the standing wave. These effects cause decoherence, but they are sufficiently small that at low levels of applied amplitude noise, quantum effects are easily observed, and at high amplitude noise levels, the applied noise dominates any effects that these other processes might have. Thus these effects do not hinder our ability to search for quantum-classical correspondence in our system.

We also note that the corrections we have mentioned lend themselves well to classical Monte Carlo simulations, whereas with other methods it would be quite cumbersome to take the many aspects of the experiment into account. A similar, quantum-mechanical analysis is much more difficult, however, since one would need to average over many wave packets in a Monte Carlo approach to obtain good convergence, and the evolution for a single quantum wave packet requires much more computation than for a single classical particle.

V. DATA AND RESULTS

A. Overview

We have undertaken a detailed experimental study of the quantum kicked rotor dynamics in the presence of amplitude noise, using the classical model for comparison. An overview of our results appears in Fig. 6, where the energies from the experiment and classical model are shown as a function of the kick strength K, for four different levels of amplitude noise. The energies are plotted at the fixed time of 35 kicks. In the case of no applied noise, one can clearly see the oscillations that correspond to Eqs. (11) and (17). Additionally, the shift in the locations of the experimental oscillations from their classical counterparts is evident; for the value of $\bar{\hbar}=2.08$ used in all the experiments shown here, the shift is 20% above the classical value. Although in some locations the quantum (experimentally observed) energies are larger than the classical (numerically calculated) energies due to the

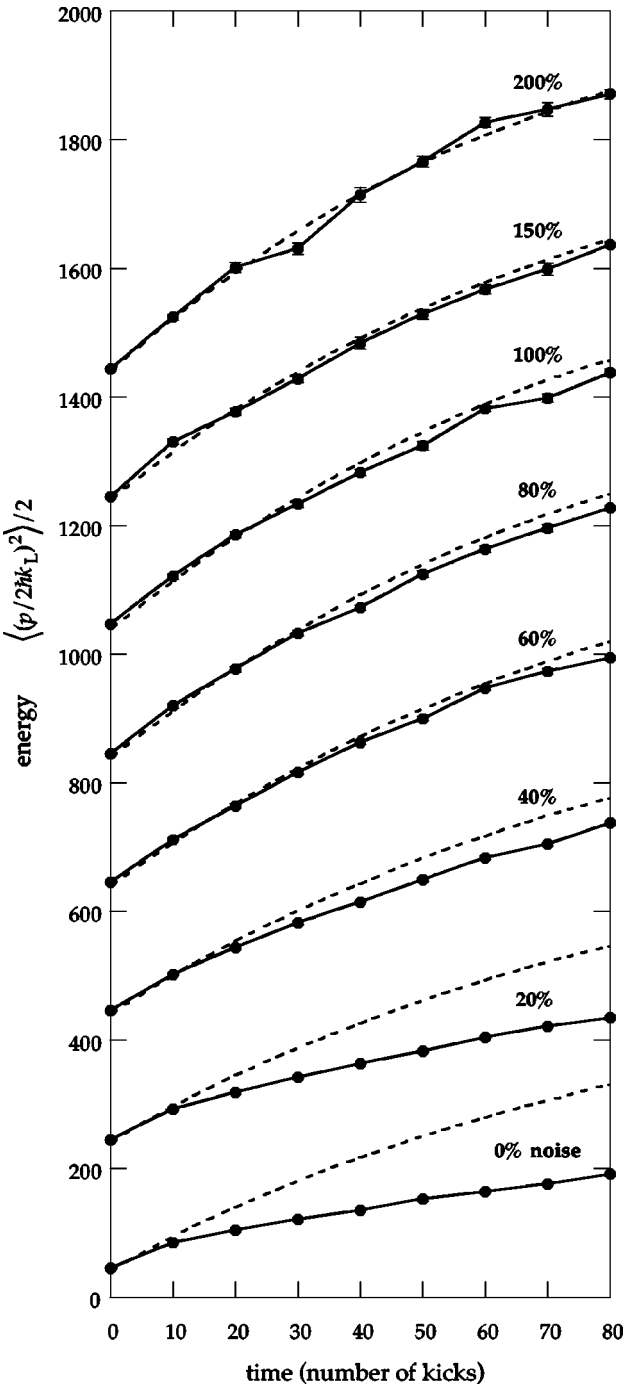

FIG. 9. Experimentally measured energy (points and solid lines) and energy from the classical model (dashed line) as a function of time, for various levels of applied noise. The experimentally measured stochasticity parameter is $K=11.2\pm10\%$, and the simulation corresponds to $K=11.2$. The experimental data points are averages over 15 distinct realizations of amplitude noise, and data for successive noise levels are offset vertically by 200 for clarity. The agreement between the experimental data and the classical model is excellent for noise levels of 60% and above. The value of K used here corresponds to the rightmost arrow in Fig. 6.

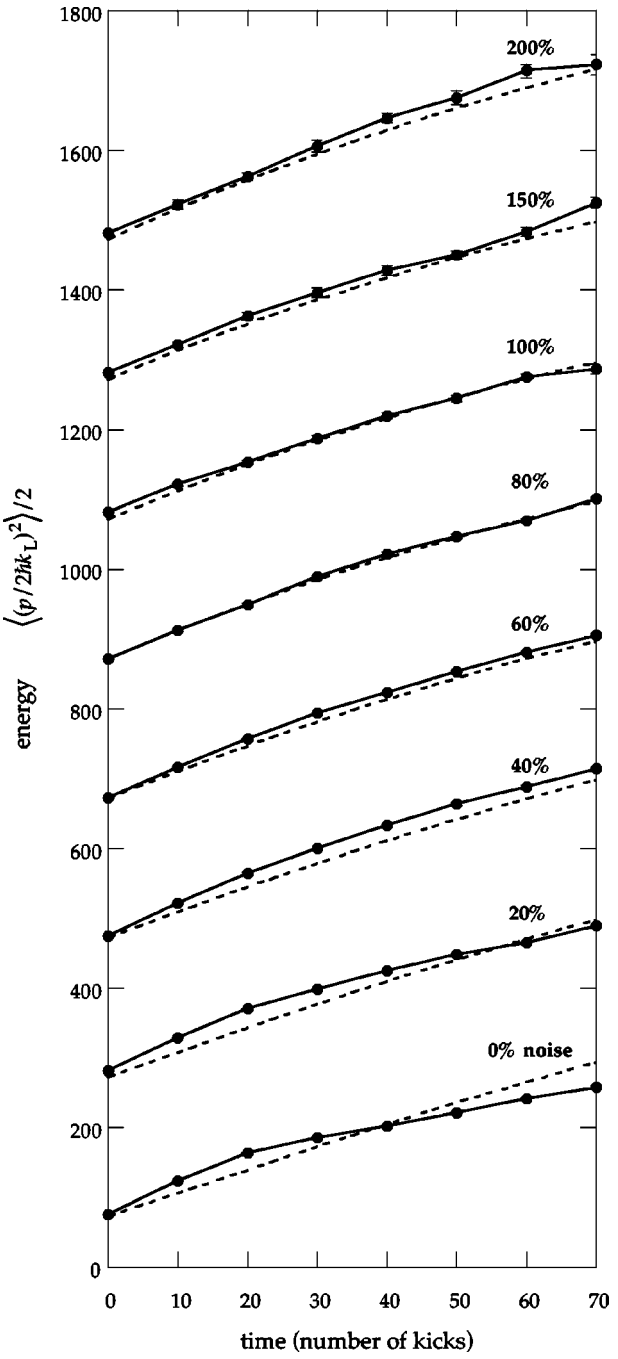

FIG. 10. Experimentally measured energy (points and solid lines) and energy from the classical model (dashed line) as a function of time, for various levels of applied noise. The experimentally measured stochasticity parameter is $K=8.4\pm10\%$, and the simulation corresponds to $K=8.7$. The experimental data points are averages over 15 distinct realizations of amplitude noise, and data for successive noise levels are offset vertically by 200 for clarity. The agreement between the experimental data and the classical model is again excellent for noise levels of 60% and above. The value of K used here corresponds to the leftmost arrow in Fig. 6.

shift of the oscillations, the experimental energies are smaller on average than the classical energies because of quantum localization effects.

As the noise is added, the oscillations in the energy curves become washed out, as one expects from Eqs. (14) and (18). Additionally, the difference between the experimental and classical curves becomes less apparent, until the highest noise level (80%), where there is excellent agreement between the two curves. In accordance with our previous discussion, good correspondence only occurs when the noise level is sufficiently large to destroy the short-time quantum

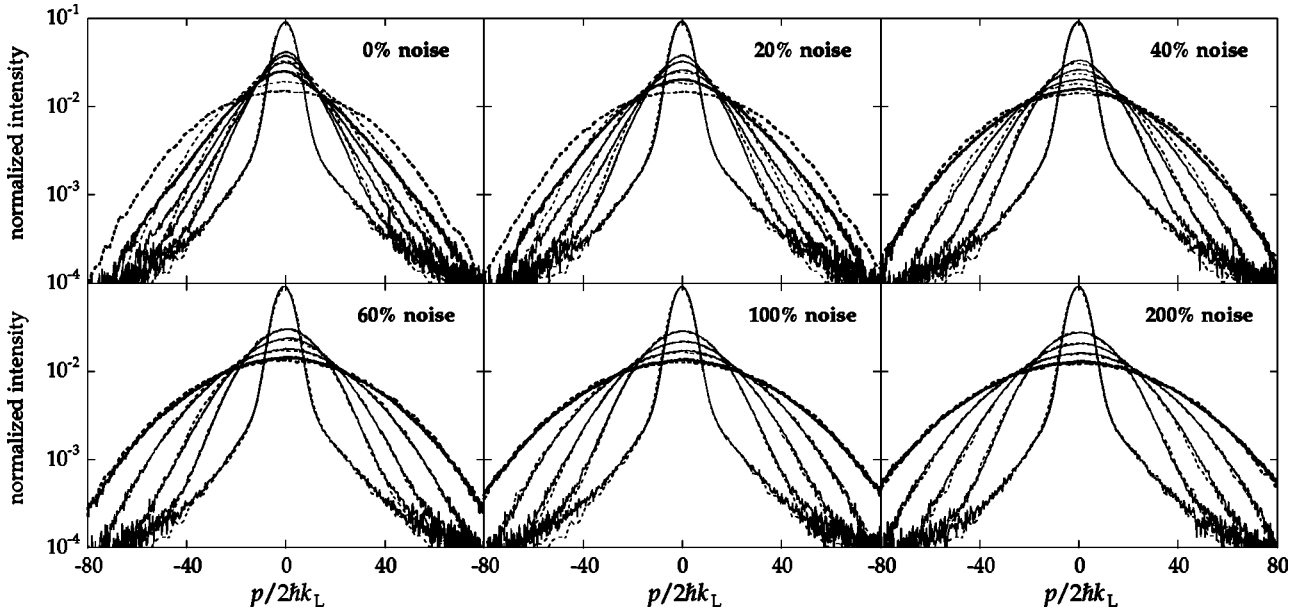

FIG. 11. Evolution of the momentum distributions, for both the experiment (solid) and classical model (dashed), at various levels of applied noise. The experimentally measured stochasticity parameter is $K=11.2\pm10\%$, and the simulation corresponds to $K=11.2$. The times shown, in order of increasing width, are 0, 10, 20, 40, and 80 kicks, with the final distributions emphasized in bold. In the zero-noise case, the contrast between the exponentially localized experimental distribution and the classical Gaussian distribution is evident. For the largest three levels of noise shown, the experimental and classical distributions are nearly indistinguishable. The data and simulations presented in this figure are the same as those used to calculate the energies in Fig. 9, and the value of K used here corresponds to the rightmost arrow in Fig. 6 (the ''valley'' in the experimental curve).

and classical correlations, and hence the oscillations in the diffusion curves.

To fill out this picture of the kicked rotor behavior, we present detailed views of the experimental and classical dynamics at two values of K in the following two subsections. The two values of K in these detailed measurements correspond to a minimum and a maximum of the quantum energy curve in Fig. 6; these locations are indicated as arrows in the

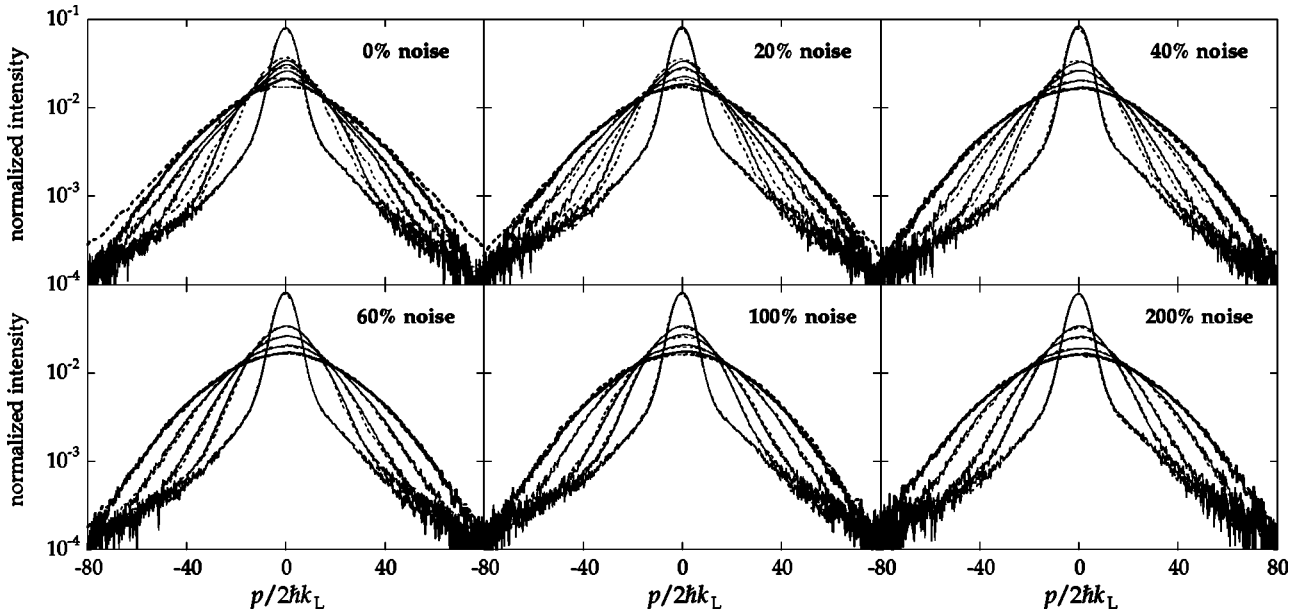

FIG. 12. Evolution of the momentum distributions, for both the experiment (solid) and classical model (dashed), at various levels of applied noise. The experimentally measured stochasticity parameter is $K=8.4\pm10\%$, and the simulation corresponds to $K=8.7$. The times shown, in order of increasing width, are 0, 10, 20, 40, and 70 kicks, with the final distributions emphasized in bold. In the zero-noise case, the quantum distribution does not exhibit exponential localization, as observed in previous work, but the behavior is distinctly nonclassical. For the largest three levels of noise shown, the experimental and classical distributions are again nearly indistinguishable. The data and simulations presented in this figure are the same as those used to calculate the energies in Fig. 10, and the value of K used here corresponds to the leftmost arrow in Fig. 6 (the ''peak'' in the experimental curve).

zero-noise plot in this figure. From previous work [48], we know that the qualitative dynamics are distinctly different at these two locations. At the minima of the experimental diffusion curve, exponential localization occurs. However, at the maxima, the late-time distributions that we measure in our experiment are nonexponential; this behavior is a fingerprint of the underlying classical anomalous diffusion.

In Figs. 7–12, we contrast the behavior of the experimental and classical systems at these two values of K. The behaviors at small noise levels have several interesting differences, but, as we have already seen, the behavior at high noise levels is similar in that there is good correspondence between the experiment and the classical simulations. In Figs. 7 and 8, we show the behaviors of the energies at the minimum and maximum of the experimental diffusion curve, respectively, at a fixed time (50 kicks) as the level of noise varies. The time evolutions of the energies are shown in Figs. 9 and 10 for the two values of K at various levels of noise. Finally, the corresponding evolutions of the momentum distributions themselves are shown in Figs. 11 and 12. We will discuss these results for the two values of K separately in the following two subsections.

Before proceeding, though, we make a few remarks about the comparisons between the experiment and the correscponding classical dynamics performed in this paper. The classical model contains many experimental parameters beyond the two that are really important for the quantum kicked rotor dynamics (K and $\bar{\kappa}$). For the purposes of comparison, we emphasize that all the extra parameters are not treated as fitting parameters; instead, they are all fixed to their experimentally measured values. However, the stochasticity parameter K, which is by far the largest source of uncertainty in our experiments, is sometimes adjusted by a few percent from its measured value (but well within the experimental uncertainty of $\pm 10\%$) in order to obtain better correspondence. To be precise about these adjustments, the measured values of K are presented in each figure caption along with the value used in the classical simulations. Finally, as noted before, although we indicate statistical error for our energy measurements in each figure, they are of limited utility in determining the quality of the correspondence between the experimental results and classical simulations. The main reason for this statement is the long-term optical alignment and laser drifts that result in long-term drifts in K, which can result in local systematic shifts in energies between different curves (or even points within a curve) in each figure. This effect is not properly accounted for by either the statistical error estimates or the simulations, which use a single value of K for an entire data set. For example, in Figs. 9 and 10, it is not possible to distinguish different levels of agreement between the data and simulations for the 60–200 % noise levels, although some pairs of curves may appear to agree more closely than others. Indeed, it is important to realize that the momentum distributions are the most reliable tool for studying correspondence, since they contain much more information, and tend to be less sensitive to the problems we have mentioned. The energies, on the other hand, are still valuable as a concise summary of the large amount of information presented here.

B. Detailed study: destruction of exponential localization

We now focus on the behavior at the minimum of the experimental diffusion curve, as indicated by the rightmost arrow in Fig. 6. In this regime, the atoms localize in an exponential distribution at late times. In Fig. 7, there is a large difference between the experimental and classical energies after 50 kicks when no noise is applied. This difference is due to both dynamical localization and the misalignment of the quantum and classical diffusion oscillations, which gives the classical system a larger initial diffusion rate. As noise is added, both the experimental data and the classical simulations exhibit increased diffusion, as the short-time correlations are washed out. The increase in the experimental diffusion is larger than the classical diffusion because quantum localization is destroyed. At high noise levels, the agreement between experiment and classical simulation is good. Additionally, both curves exhibit a characteristic dip in the energy around 150% noise levels. This somewhat surprising effect is a result of residual short-time correlations, which persist at noise levels as high as 100%, where they enhance diffusion slightly above the quasilinear value.

Similar behavior occurs in the time evolution of the energies shown in Fig. 9. When there is no applied noise, the experimental energy grows initially more slowly than the classical energy, and then saturates and diffuses slowly. This slow diffusion is likely due to residual decohering effects in our experiment, such as phase noise in the standing wave. As noise is added, the diffusion is enhanced in both cases, and for high noise levels the energy growth in the experiment is quite similar to that observed in the simulations.

Finally, the transition to classical behavior in the experiment is most dramatically evident in the momentum distributions shown in Fig. 11. In the zero-noise case, the experimental distributions evolves from the initial, nearly Gaussian form to the exponentially localized distribution (shown in bold), which is characteristic of dynamical localization. The classical distribution, on the other hand, evolves to the broader, Gaussian distribution that one expects from classical physics. When a small amount of noise (20%) is applied, the final experimental distribution is broader and has a rounded appearance, but is still quite far away from the classical Gaussian distribution. With 40% noise, the final experimental distribution has made the transition to a Gaussian profile, but the widths still do not quite match the classical predictions. For the highest levels of noise shown (60–200 %), the evolutions of the experimental and classical distributions are nearly identical, providing strong evidence that the experiment is behaving classically.

C. Detailed study: regime of classical anomalous diffusion

In this section, we focus on a different regime than in Sec. V B. Here we consider the behavior at a peak in the experimental diffusion curve, indicated by the leftmost arrow in Fig. 6. This location in the diffusion curve corresponds to a regime of classical anomalous diffusion. As in the previous case, there is a significant difference in the energy after 50 kicks in the absence of noise, as seen in Fig. 8. The difference in this figure is much larger than in Fig. 6, because of the much later time used in the plot (50 vs 35 kicks). As noise is applied, the experimental energy increases. This be-

havior is consistent with the breaking of localization, although it is not completely clear that localization occurs in this regime, because of the nonexponential form of the long-time momentum distributions. By contrast, the classical energy is initially reduced by the applied noise, due to the destruction of the classical correlations. Again, for high noise levels the behavior in the experiment is well described by the classical model.

From the evolution of the energies in Fig. 10, we see that the differences between the behaviors of the atoms and the classical model are more subtle than in the case of Sec. V B. When there is no applied noise, the experimental data show a faster initial diffusion than one would expect classically; at later times, the diffusion seems to saturate, suggesting that localization effects are setting in, and the diffusion proceeds more slowly than in the classical model. The energy difference in this case is smaller than one might expect from Fig. 8, due to slight differences in the intensity and beam diameter of the kicking laser light between the two data runs (note that this value of K corresponds to a steeply sloped region in the classical diffusion curve). As noise is added, the saturation is less pronounced, until at 40% noise, where the diffusion occurs more quickly than in the classical model, with little indication of saturation. Above this level, the experiment agrees well with the classical model, and the short-time correlations are evidently small.

The momentum distributions for this case are shown in Fig. 12. In the zero-noise case, the experimental distribution after 70 kicks (highlighted in bold) has a characteristic profile, rounded and nonexponential in shape. One might be tempted to attribute this shape to the systematic effects that we have discussed, which affect the tails of an exponential distribution with a very long localization length. However, the region over which the distribution is rounded is well within the domain where the systematic effects are not significant. The final classical distribution also has tails that extend well beyond those of the experimental measurement. As noise is introduced, the experimental profile becomes more Gaussian, and the classical diffusion rate is reduced slightly. As in Sec. V B, the final experimental distribution for 40% noise is Gaussian, but the evolution does not quite proceed at the same rate (as one can most readily see from the distributions at intermediate times). The difference, though, is that the quantum diffusion occurs more quickly than the classical expectation, whereas in Sec. V B the diffusion occurred more slowly than in the classical model. Again, for the highest levels of noise shown (60–200 %), the experimental evolutions are in excellent agreement with the classical model, and hence classical behavior is restored.

VI. SUMMARY

We have presented a detailed study of the transition to classical behavior in an experimental realization of the quantum kicked rotor system. An important component in the analysis of this transition is a meticulous understanding of how various aspects of the experimental system affect the measured evolution of the atoms. We have observed that for sufficiently high levels of noise, the global behavior of the experimental system is in good agreement with a classical model of the experiment, which includes the effects of the noise as well as the most significant aspects of the experimental setup.

There is still much interesting work to be done in this area, and there are several future directions for this experiment that are directly related to the work discussed here. First, it appears that the quantum behavior is relatively robust to the applied noise, most likely because of the strongly quantum nature of our parameter regime. It would be interesting to compare the effects of different types of noise in the experiment, to see if the system is especially sensitive to any particular form of noise. Another possibility would be to operate in a more classical regime (smaller $\hbar$), where the kicked rotor should be more susceptible to noise. In this regime, it should also be possible to observe quantum-classical correspondence without destroying the short-time correlations, since there would be little mismatch between the quantum and classical diffusion oscillations. Finally, we will soon have the ability to prepare localized initial conditions in phase space, and it will be possible to study the effects of noise on local phase space structures.

ACKNOWLEDGMENTS

The authors thank Cyrus Bharucha for a careful reading of the manuscript. This work was supported by the Robert A. Welch Foundation and the National Science Foundation. D.A.S. acknowledges support from the Fannie and John Hertz Foundation. Computations were performed on Texas Advanced Computing Center supercomputers.

[1] R. Blümel and W. P. Reinhardt, *Chaos in Atomic Physics* (Cambridge University Press, Cambridge, 1997).
[2] Wojciech Hubert Zurek and Juan Pablo Paz, Phys. Rev. Lett. **72**, 2508 (1994).
[3] K. Shiokawa and B.L. Hu, Phys. Rev. E **52**, 2497 (1995).
[4] E. Ott, T.M. Antonsen, Jr., and J.D. Hanson, Phys. Rev. Lett. **53**, 2187 (1984).
[5] T. Dittrich and R. Graham, Europhys. Lett. **4**, 263 (1987).
[6] S. Fishman, and D.L. Shepelyansky, Europhys. Lett. **16**, 643 (1991).
[7] Doron Cohen, Phys. Rev. A **44**, 2292 (1991).
[8] S. Dyrting and G.J. Milburn, Phys. Rev. A **51**, 3136 (1995).
[9] Jiangbin Gong and Paul Brumer, Phys. Rev. E **60**, 1643 (1999).
[10] R. Blümel, R. Graham, L. Sirko, U. Smilansky, H. Walther, and K. Yamada, Phys. Rev. Lett. **62**, 341 (1989); M. Arndt, A. Buchleitner, R.N. Mantegna, and H. Walther, *ibid.* **67**, 2435 (1991); R. Blümel, A. Buchleitner, R. Graham, L. Sirko, U. Smilansky, and H. Walther, Phys. Rev. A **44**, 4521 (1991); O. Benson, A. Buchleitner, G. Raithel, M. Arndt, R.N. Mantegna, and H. Walther, *ibid.* **51**, 4862 (1995).
[11] James E. Bayfield, Chaos **1**, 110 (1991).
[12] L. Sirko, M.R.W. Bellermann, A. Haffmans, P.M. Koch, and D. Richards, Phys. Rev. Lett. **71**, 2895 (1993).

[13] Peter M. Koch, Physica D **83**, 178 (1995).
[14] L. Sirko, A. Haffmans, M.R.W. Bellermann, and P.M. Koch, Europhys. Lett. **33**, 181 (1996).
[15] R.M. Clarke, I.H. Chan, C.M. Marcus, C.I. Duruöz, J.S. Harris, Jr., K. Campman, and A.C. Gossard, Phys. Rev. B **52**, 2656 (1995).
[16] B.G. Klappauf, W.H. Oskay, D.A. Steck, and M.G. Raizen, Phys. Rev. Lett. **81**, 1203 (1998); **82**, 241(E) (1999).
[17] H. Ammann, R. Gray, I. Shvarchuck, and N. Christensen, Phys. Rev. Lett. **80**, 4111 (1998); also see the Comment by S. Habib, H. Mabuchi, K. Shizume, and B. Sundaram (unpublished).
[18] M.S. Chapman, T.D. Hammond, A. Lenef, J. Schmiedmayer, R.A. Rubenstein, E. Smith, and D.E. Pritchard, Phys. Rev. Lett. **75**, 3783 (1995).
[19] M. Brune, E. Hagley, J. Dreyer, X. Maître, A. Maali, C. Wunderlich, J.M. Raimond, and S. Haroche, Phys. Rev. Lett. **77**, 4887 (1996).
[20] C. Monroe, D.M. Meekhof, B.E. King, and D.J. Wineland, Science **272**, 1131 (1996).
[21] R. Graham, M. Schlautmann, and P. Zoller, Phys. Rev. A **45**, R19 (1992).
[22] F.L. Moore, J.C. Robinson, C. Bharucha, P.E. Williams, and M.G. Raizen, Phys. Rev. Lett. **73**, 2974 (1994).
[23] J.C. Robinson, C. Bharucha, F.L. Moore, R. Jahnke, G.A. Georgakis, Q. Niu, M.G. Raizen, and Bala Sundaram, Phys. Rev. Lett. **74**, 3963 (1995).
[24] F.L. Moore, J.C. Robinson, C.F. Bharucha, Bala Sundaram, and M.G. Raizen, Phys. Rev. Lett. **75**, 4598 (1995).
[25] B.G. Klappauf, W.H. Oskay, D.A. Steck, and M.G. Raizen, Physica D **131**, 78 (1999).
[26] J.P. Gordon and A. Ashkin, Phys. Rev. A **21**, 1606 (1980).
[27] B.V. Chirikov, Phys. Rep. **52**, 264 (1979).
[28] A.B. Rechester and R.B. White, Phys. Rev. Lett. **44**, 1586 (1980).
[29] A.B. Rechester, M.N. Rosenbluth, and R.B. White, Phys. Rev. A **23**, 2664 (1981).
[30] A. J. Lichtenberg and M.A. Lieberman, *Regular and Chaotic Dynamics* (Springer-Verlag, New York, 1992).
[31] Joseph Klafter, Michael F. Schlesinger, and Gert Zumofen, Phys. Today **49**(2), 33 (1996).
[32] B.V. Chirikov and D.L. Shepelyansky, Physica D **13**, 395 (1984).
[33] T. Geisel, A. Zacherl, and G. Radons, Phys. Rev. Lett. **59**, 2503 (1987); B.V. Chirikov and D.L. Shepelyansky, *ibid.* **61**, 1039 (1988); T. Geisel, A. Zacherl, and G. Radons, *ibid.* **61**, 1040 (1988).
[34] S. Benkadda, S. Kassibrakis, R.B. White, and G.M. Zaslavsky, Phys. Rev. E **55**, 4909 (1997).
[35] Bala Sundaram and G.M. Zaslavsky, Phys. Rev. E **59**, 7231 (1999).
[36] G.M. Zaslavsky, M. Edelman, and B.A. Niyazov, Chaos **7**, 159 (1997).
[37] George M. Zaslavsky, Phys. Today **52**(8), 39 (1999).
[38] Alexander I. Saichev and George M. Zaslavsky, Chaos **7**, 753 (1997).
[39] R. Blümel, S. Fishman, and U. Smilansky, J. Chem. Phys. **84**, 2604 (1986).
[40] G. Casati, B. V. Chirikov, J. Ford, and F. M. Izrailev, *Stochastic Behaviour in Classical and Quantum Hamiltonian Systems*, edited by G. Casati and J. Ford, Lecture Notes in Physics Vol. 93 (Springer, Berlin, 1979).
[41] D.L. Shepelyansky, Physica D **8**, 208 (1983).
[42] T. Hogg and B.A. Huberman, Phys. Rev. Lett. **48**, 711 (1982).
[43] Shmuel Fishman, D.R. Grempel, and R.E. Prange, Phys. Rev. Lett. **49**, 509 (1982).
[44] D.R. Grempel, R.E. Prange, and Shmuel Fishman, Phys. Rev. A **29**, 1639 (1984).
[45] Shmuel Fishman, in *Quantum Dynamics of Simple Systems: The Forty-Fourth Scottish Universities Summer School in Physics, Stirling, 1994*, edited by G. L. Oppo, S. M. Barnett, E. Riis, and M. Wilkinson (Scottish Universities Summer School in Physics & Institute of Physics Publishing, Bristol, 1996).
[46] D.L. Shepelyansky, Theor. Math. Phys. **49**, 925 (1982).
[47] D.L. Shepelyansky, Physica D **28**, 103 (1987).
[48] B.G. Klappauf, W.H. Oskay, D.A. Steck, and M.G. Raizen, Phys. Rev. Lett. **81**, 4044 (1998).
[49] Steven Chu, Science **253**, 861 (1991).
[50] W. Petrich, M.H. Anderson, J.R. Ensher, and E.A. Cornell, J. Opt. Soc. Am. B **11**, 1332 (1994).
[51] C.G. Townsend, N.H. Edwards, C.J. Cooper, K.P. Zetie, C.J. Foot, A.M. Steane, P. Szriftgiser, H. Perrin, and J. Dalibard, Phys. Rev. A **52**, 1423 (1995).